

NUMERICAL SOLUTION OF LOX FLOW IN A LIQUID ROCKET ENGINE ADDITIVELY MANUFACTURED COOLING CHANNEL

Nikos Monokrousos[1], László Könözsy[1], Vassilios Pachidis[1], Ernesto Sozio[2] & Federico Rossi[2]

[1]Cranfield University, College Road, Cranfield, Bedfordshire, MK430 AL, United Kingdom
[2]Pangea Aerospace, Avinguda Número 1, 20 08040 Barcelona, Spain

Abstract

The present work has been conducted in the framework of the DemoP1 demonstrator for the design of a LOx/LNG aerospike engine carried out by Pangea Aerospace. The main objective of the demonstrator is to highlight the central features of the next generation booster-class engines such as reusability, the utilisation of cryogenic coolants and the benefits arising from the ever-growing field of Additive Manufacturing (AM) for high heat flux aerospace applications with increasing thermal load management demands. In the present study a numerical investigation of the cryogenic liquid oxygen coolant flow in an AM cooling channel of the DemoP1 engine is implemented. The simulations are performed on a three-dimensional curvilinear cooling channel of variable, rectangular cross-section of the aerospike engine. Different variations of the two-equation $k-\omega$ turbulence model are employed and assessed for the closure of the fluid flow governing equations and the identification of the efficient formulations for the accurate prediction of the spatial development of the primitive variables. The numerical solutions obtained for the characterisation of heat transfer and pressure drop in the AM cooling channel are compared against experimental data provided from Pangea Aerospace for the full-scale single-injector element hot-fire test campaign of the DemoP1 aerospike engine demonstrator.

Keywords: aerospike engine, additive manufacturing, cooling channel, two-equation $k-\omega$ turbulence model

1. Introduction

1.1 Additive Manufacturing for high heat flux aerospace applications

There has always been an increased effort for the development of propulsion systems related to high-speed civil transportation and more efficient access to space. Traditional systems are usually linked with rocket-based applications and many studies focus on their investigation either from a numerical [1, 2] or an experimental point of view [3]. However several air-breathing concepts utilising pre-cooling technology have also been examined [4] as an alternative propulsion system exhibiting improved efficiency over chemical rockets [5, 6]. While these concepts could drastically reduce the associated cost for space access due to improved thermodynamic efficiency, their aerodynamic behavior is not yet well-understood especially at the exhaust region of the nozzle [7]. Most of the experimental effort focused on exhaust nozzle aerodynamics is based on cold-flow testing [8, 9] owing to the increased cost and facility-related limitations and constraints of hot-flow experimental campaigns. Nevertheless, hot-flow testing is required to comprehend the effect of heat fluxes on the investigated flow-field characteristics and the determination of a strategy for the thermal load demands management. The recent advances in the field of Additive Manufacturing (AM) is an apparent consequence of the growing interest shown for the development of high heat flux aerospace applications.

The manufacturing of metallic components of complex geometric configurations such as regenerative cooling systems and combustion chambers of liquid rocket engines has benefited greatly from the rapid growth of Additive Manufacturing (AM) technologies [10]. In comparison with conventional technologies AM offers great advantages in the manufacturing process in terms of the integration of the metal component directly to the main body [11], the high degree of freedom it allows in the design

process [12] and the calibrating capabilities for the determination of the maximum amount of heat transfer whilst retaining low pressure drop values in high-temperature applications [13]. Other benefits of AM technologies regard the reduced material and weight of the produced metal component yielding an overall reduction in the manufacturing cost. However, the limitations of the AM processes should not, in any case, be disregarded. A significant disadvantage of the production of metal components through an AM process is the effect of the manufacturing process on the mechanical strength and properties of the material due to the formation of microstructures and porosities [14]. Attention has also been brought to liquid rocket engine metallic components of large volume due to possible scalability restrictions arising from the employed additive manufacturing technique [15]. Ultimately the high, non-uniform, process-inherited roughness on the wall boundaries constitutes the greatest challenge for the characterisation of heat transfer and pressure drop in an AM channel [16].
Current trends in the field of Additive Manufacturing (AM) suggest the utilisation of copper-based alloys for high heat flux aerospace applications due to the increased thermal conductivity and mechanical properties of the alloys [17]. A promising copper alloy candidate for the manufacturing of metallic components such as combustion chambers with a regenerative cooling system is the GRCop-42 [10, 18]. The GRCop-42 copper alloy consists of Cu-4 at.%Cr-2 at.%Nb and Fe, O, Al and Si in smaller concentrations. Experimental data on its thermophysical and mechanical properties are available in the literature [10, 19]. A detailed review of different processes for the additive manufacturing of copper-chromium-niobium alloys such as the GRCop-42 alloy can be found in [20].

1.2 Additive Manufacturing for liquid rocket engine cooling channels

Liquid rocket engine Additively Manufactured (AM) cooling channels have only recently started being studied. The HYPROB program carried out by CIRA, the Italian Aerospace Research Center under contract with the Italian Ministry of Research has been a characteristic example for the design of an experimental campaign of a liquid rocket engine cooling system focused on LOx/LCH_4 propellants [21]. Several computational studies have been conducted within this experimental campaign on numerical building activities for the investigation and modelling of the behavior of methane in the rectangular cross-section cooling channels of the regenerative cooling system. A three-dimensional conjugate heat transfer model has been implemented for the characterisation of the coolant behavior in near-critical conditions and under the influence of different coolant pressure and surface roughness values on the wall boundaries [22]. The results indicated the significance of heat transfer phenomena such as heat transfer deterioration resulting from the coolant operation in near-critical conditions. Supplementary results for the experimental campaign with respect to the pressure drop and the heat transfer characteristics are also reported in [23, 24]. High roughness channel flows have also been investigated within the HYPROB program for the construction of a model for the accurate prediction of heat transfer. The numerical investigation of Latini et al. [25] focused on the extension of the external flows roughness correction of the one-equation Spalart-Allmaras turbulence model to account for phenomena arising in high roughness internal flows. In addition to studies conducted within the HYPROB program, the characterisation of the convective heat transfer and pressure drop has been investigated in rectangular cross-section AM minichannels [16] and microchannels [26].
The utilisation of Additive Manufacturing (AM) techniques for high heat flux aerospace applications involving the manufacturing of liquid rocket engine components such as thrust chambers or regenerative cooling systems is evident. Currently various industrial companies redirect their research and development activities on the additive manufacturing of metallic components. A comprehensive review on the importance and the advantages that AM technologies offer to the current space economy section can be found in [27]. A novel concept combining AM techniques and aerospace applications of high heat flux requirements has been the design of the DemoP1, a 20 [kN] thrust LOx/LNG aerospike engine demonstrator carried out by Pangea Aerospace [28]. The motivation for the design of the DemoP1 aerospike engine is to highlight the main features of the next generation booster-class engines such as reusability, the operation of the regenerative cooling system using cryogenic coolants and the beneficial features arising from the ever-growing field of additive manufacturing for aerospace applications with increasing thermal load management requirements [28].
A dual regenerative cooling system is integrated in the DemoP1 demonstrator for the satisfaction of the increased thermal load demands encountered across the engine and especially at the throat

region. The dual regenerative cooling system is based on counterflowing liquid oxygen in AM cooling channels through the central plug starting from the base up to the injector head, in addition to cooling the external housing by flowing liquid natural gas in the cooling channels surrounding it. Fadigati et al. [29] presented numerical results for the characterisation of the external flow-field and the determination of the pressure distribution and heat transfer characteristics of the DemoP1 aerospike engine demonstrator. After careful considerations GRCop-42 copper-based alloy was selected for the additive manufacturing of the engine demonstrator using the Selective Laser Melting (SLM) manufacturing technique. Large values of surface roughness characterised by high non-uniformity are inherited from the AM process and are expected to aim the cooling capabilities of the dual regenerative cooling system on the penalty of larger pressure drop across the AM cooling channels. A review of the research activities for the development of the DemoP1 aerospike engine demonstrator can be found in [28]. Details on the manufacturing process of the DemoP1 engine and the full-scale single-injector hot-fire testing campaign performed are described in [30]. In the current work a numerical investigation for the solution of liquid oxygen flow in an AM cooling channel of the DemoP1 aerospike engine demonstrator designed by Pangea Aerospace is presented. Different variations of the two-equation $k-\omega$ turbulence model and roughness modelling approaches are employed for the assessment of their performance to accurately capture the flow-field and heat transfer characteristics of the cryogenic coolant. The resulted numerical solutions are compared against experimental measurements obtained from the hot-fire testing campaign of the DemoP1 aerospike engine.

2. Methodology

For the numerical solution of liquid oxygen in the Additively Manufactured (AM) cooling channel of the DemoP1 aerospike engine demonstrator designed by Pangea Aerospace specific numerical building activities have been implemented. In this section the mass (continuity), momentum and energy conservation equations governing the coolant flow in the AM liquid rocket engine channel are presented as well as information on the employed turbulence models for the Reynolds-Averaged Navier-Stokes (RANS) closure problem and the determination of the turbulence transport quantities. The numerical implementation details for the computational setup of the required simulations are also reported in addition to the process followed for the estimation of the equivalent sand-grain roughness height on the wall boundaries of the AM cooling channel. Lastly a grid sensitivity analysis is carried out for the determination of an appropriate grid size. In the next section the results of the performed numerical simulations employing different variations of the two-equation $k-\omega$ turbulence model for the liquid oxygen flow in the AM cooling channel of the DemoP1 aerospike engine demonstrator are reported.

2.1 Governing equations and closure model

The system of governing equations for the steady-state numerical solution of the coolant flow in the Additively Manufactured (AM) cooling channel of the DemoP1 engine consists of the mass (continuity), momentum and energy conservation Navier-Stokes equations. Under the assumption of no external forces applying on the fluid the three-dimensional governing flow equations are written as

$$\frac{\partial}{\partial x_i}\left(\rho u_i\right) = 0, \tag{1}$$

$$\frac{\partial}{\partial x_j}\left(\rho u_i u_j\right) = -\frac{\partial P}{\partial x_i} + \frac{\partial}{\partial x_j}\left[\mu\left(\frac{\partial u_i}{\partial x_j} + \frac{\partial u_j}{\partial x_i} - \frac{2}{3}\delta_{ij}\frac{\partial u_i}{\partial x_j}\right)\right] + \frac{\partial}{\partial x_j}\left(-\rho\overline{u_i' u_j'}\right), \tag{2}$$

$$\frac{\partial}{\partial x_j}\left[u_i\left(\rho E + p\right)\right] = \frac{\partial}{\partial x_j}\left[\left(\lambda + \frac{c_p \mu_t}{Pr_t}\right)\frac{\partial T}{\partial x_j} + u_i\left(\tau_{ij}\right)_{eff}\right], \tag{3}$$

where $i = 1,2,3$ is the coordinate direction, u_i the velocity component in each direction, ρ the fluid density, P the static pressure, μ the fluid dynamic viscosity, δ_{ij} the Kronecker delta and E the total energy defined as $E = c_p T - \frac{p}{\rho} + \frac{u^2}{2}$. Thermal conductivity is represented as λ, c_p is the specific heat capacity at constant pressure, μ_t the turbulent (eddy) dynamic viscosity, Pr_t the turbulent Prandtl number, T the static temperature and $\left(\tau_{ij}\right)_{eff}$ is the deviatoric stress tensor for $j \neq i$ defined as

$$\left(\tau_{ij}\right)_{eff} = \mu_{eff}\left(\frac{\partial u_j}{\partial x_i} + \frac{\partial u_i}{\partial x_j}\right) - \frac{2}{3}\mu_{eff}\frac{\partial u_i}{\partial x_j}\delta_{ij}. \tag{4}$$

The solution of the liquid oxygen flow in the AM cooling channel of the DemoP1 aerospike engine demonstrator is implemented in the ANSYS Fluent 2023 R2 commercial CFD package [31]. In the present study different variations of the two-equation $k-\omega$ turbulence model are employed for the closure problem of the Reynolds-Averaged Navier-Stokes (RANS) problem and assessed for the numerical solution of the coolant flow in the AM cooling channel. The variations of the two-equation $k-\omega$ turbulence model are the following: a) the standard $k-\omega$ turbulence model of D. C. Wilcox [32], b) the baseline $k-\omega$ turbulence model of F. R. Menter [33] and c) the $k-\omega$ shear stress transport (SST) model [33]. The main drawback of the standard $k-\omega$ turbulence model is the sensitivity of the k and ω transport quantities outside of the shear layer notably in the case of free shear flows [34]. Details for the numerical implementation of the transport equations and model constants for the standard two-equation $k-\omega$ turbulence model can be found in [32]. The baseline two-equation $k-\omega$ turbulence model consists one of the first approaches to combine the beneficial features of employing the standard $k-\omega$ turbulence model for the resolution of the near-wall region and the two-equation $k-\varepsilon$ turbulence model at the outer region [34]. Comparing to the standard version of the $k-\omega$ model, the baseline model integrates a blending function for the activation of either the ω-based treatment at the near-wall region or the ε-based treatment away from the wall boundary. An additional term representing the damped cross diffusion is introduced in the specific dissipation rate transport equation whereas the baseline $k-\omega$ model contains additional model constants in comparison with the standard version. The increased capabilities of the two-equation $k-\omega$ SST model regard the consideration of turbulence shear stress transport in the estimations for the determination of the fluid turbulent viscosity. The $k-\omega$ SST turbulence model has been previously employed for the solution of internal turbulent flows in rough channels with rather promising results [23]. In the present work the variations of the two-equation $k-\omega$ turbulence model are examined for the numerical solution of liquid oxygen in the AM cooling channel of the DemoP1 aerospike engine demonstrator.

2.2 Numerical setup

The three-dimensional computational fluid dynamics (CFD) approach implemented in the current work is based on an implicit, density-based method for the numerical solution of the steady-state compressible Reynolds-Averaged Navier-Stokes (RANS) equations coupled with different variations of the two-equation $k-\omega$ turbulence model. The thermophysical properties of the fluid are determined as follows: density is estimated based on the ideal gas law, specific heat capacity at constant pressure using a fifth-order polynomial with respect to the static temperature, thermal conductivity using the kinetic theory and for the definition of the dynamic viscosity of the fluid Sutherland's law is employed. The solid material properties of GRCop-42 copper-based alloy are constant with temperature and are estimated in the standard room temperature $298.2\ [K]$ as: $\rho_w = 8777.387\ [kgm^{-3}]$, $c_{p,w} = 383.841\ [Jkg^{-1}K^{-1}]$ and $k_w = 381.121\ [Wm^{-1}K^{-1}]$. Since the GRCop-42 alloy material is currently unavailable on ANSYS Fluent 2023 R2, for the determination of the constant solid material properties a combination of the thermophysical properties of the alloying metals has been implemented based on available experimental data on the density [35, 36], specific heat capacity at constant pressure [37, 38] and thermal conductivity [39]. The numerical discretisation of the governing and transport equations is performed as follows: a Roe Approximate Riemann Solver (ARS) [40] is selected for the discretisation of the convective fluxes and second-order accurate upwind schemes are employed for pressure, momentum, energy and the transport quantities of the $k-\omega$ turbulence model. With the exception of the convergence criterion for the energy residuals set equal to 10^{-12}, the convergence criterion for the remaining residuals is set equal to 10^{-8}. Similarly to the fluid reference values being computed from the inlet of the AM cooling channel, the solution is initialised using the standard initialisation method from the inlet section in a reference frame relative to the cell zone. The total number of iterations performed for each numerical simulation is equal to $3 \cdot 10^4$.

The three-dimensional geometric configuration of the AM cooling channel consists of the inlet, outlet section and the wall boundaries. The experimental measurements obtained from the hot-flow testing campaign of the DemoP1 engine are imposed in the form of boundary conditions on the commercial CFD package. A fixed mass flow rate equal to $\dot{m} = 0.076\ [kgs^{-1}]$ is imposed at the inlet section of the channel in addition to a uniform temperature profile $T = T_{in} = 107.4\ [K]$. A pressure boundary condition is employed for the outlet section equal to the experimentally measured value $P = P_{out} = 57.09\ [bar]$.

Note that the accuracy of the pressure sensors is reported as $\pm 0.8\ [bar]$ and the accuracy of the temperature sensors as $\pm 7\ [K]$. No-slip boundary conditions are imposed for the velocity components at the wall boundaries of the cooling channel. The bottom (basement) wall boundary is heated from the hot-gas side of the DemoP1 aerospike engine demonstrator. The heat flux at the top and lateral walls is set equal to zero. For the determination of the coolant-side wall temperature the solution of the one-dimensional Fourier equation for heat conduction is obtained. The hot-gas side heat transfer coefficient and adiabatic wall temperature are estimated and the hot-gas side wall temperature is assumed to be uniform and equal to $T_{w,hg} = 800\ [K]$. The width of the solid material is equal to $1\ [mm]$. The analysis presented in the current work is uncoupled with respect to the solid material wall conduction and the coolant-side estimations. Through the solution of the one-dimensional Fourier equation for the heat conduction the temperature profile of the coolant-side wall is obtained. For the integration of the resulted profile into the commercial CFD package the profile is split into three intervals and different regression models are employed to obtain a fit to the curve of the coolant-side wall temperature profile. Curve fitting was implemented on the Curve Fitter toolbox of MATLAB R2022a [41] and the details on the regression model characteristics are summarised in Table 1.

	Regression model	Number of terms	R^2	Root-mean-square error (RMSE)
Interval 1	Fourier	4	0.9999	0.01277
Interval 2	Fourier	8	0.9981	0.5574
Interval 3	Exponential	2	1	$1.17{\cdot}10^{-13}$

Table 1 – Regression model characteristics for curve fitting of coolant-side wall temperature profile.

The coolant-side wall temperature profile resulting from the numerical solution of the one-dimensional Fourier's law for the heat conduction in the solid material and the curve obtained from the regression models employed for the curve fitting are exhibited in Fig. 1. The longitudinal coordinate-dependent correlation for the coolant-side wall temperature profile is integrated into the ANSYS Fluent CFD software in the form of a User-Defined Function (UDF). It is then imposed as a thermal boundary condition for the heated bottom (basement) wall of the additively manufactured cooling channel.

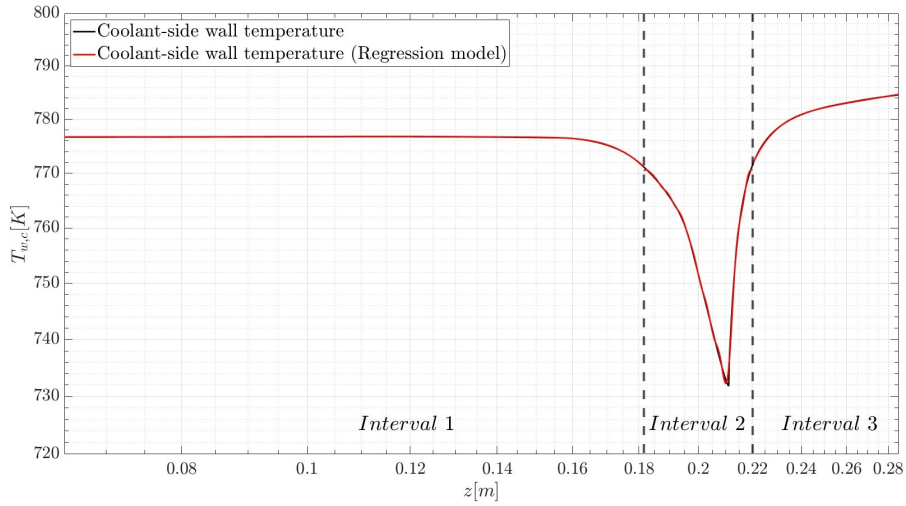


Figure 1 – Coolant-side wall temperature profile and curve fitting regression model.

2.3 Geometric configuration and surface roughness

The Additively Manufactured (AM) cooling channel of the DemoP1 aerospike engine demonstrator is a three-dimensional curved channel of variable, rectangular cross-section. The geometric configuration of the liquid oxygen AM cooling channel of the aerospike engine can be seen in Fig. 2.
In Fig. 3 the variation of the hydraulic diameter across the AM cooling channel is exhibited against the longitudinal coordinate of the channel by obtaining geometrical measurements from twelve different



Figure 2 – Geometric configuration of liquid oxygen AM cooling channel of the DemoP1 aerospike engine demonstrator designed by Pangea Aerospace.

cross-sections uniformly distributed across the channel. Note that the inlet section of the AM channel is represented at the right of the figures while the outlet section at the left side. It can be seen that the cross-section varies across the channel with the reduction of the fluidic width being obvious at the throat region to withstand the increased thermal load applied at the throat of the cooling channel [28].

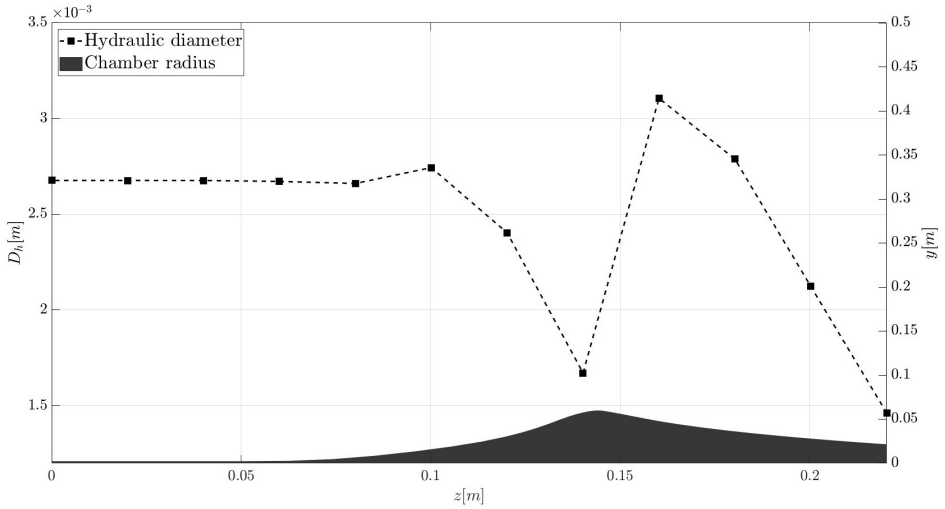


Figure 3 – Hydraulic diameter variation at different cross-sections across longitudinal coordinate of coolant side.

For the determination of the equivalent sand-grain roughness height imposed as a boundary condition on the walls of the AM cooling channel of the DemoP1 demonstrator, optical profilometry measurements were obtained from an AM sample of the demonstrator. The experimental values from the optical profilometry process for the arithmetic mean deviation (R_a), the root-mean-square roughness (R_q) and the maximum peak to valley height of the profile (R_z) in addition to the corresponding computed values based on the analysis provided from Leach [42] are summarised in Table 2.

	Optical profilometry (μm)	Leach [42] (μm)	Error
R_a	9.282	9.572	3.12%
R_q	11.449	12.175	6.34%
R_z	49.888	75.003	50.34%

Table 2 – Statistical surface roughness parameters based on experimental and computed data.

The evaluation profile obtained with respect to a height distribution function (HDF) of the rough elements of the sample can be seen in Fig. 4. The origin for the evaluation of the arithmetic mean deviation (R_a) and the root-mean-square roughness (R_q) is the mean line of the evaluation profile exhibited in Fig. 4. The percentage error between the obtained values is also reported in Table 2. It is shown that although the percentage error for the R_a and R_q roughness parameters is within an acceptable range, the error between the measured R_z parameter and the parameter value computed

from the sample evaluation profile is 50.34%. Note that large uncertainty values on the R_z statistical surface roughness parameter have been reported in previous experimental investigations [26].

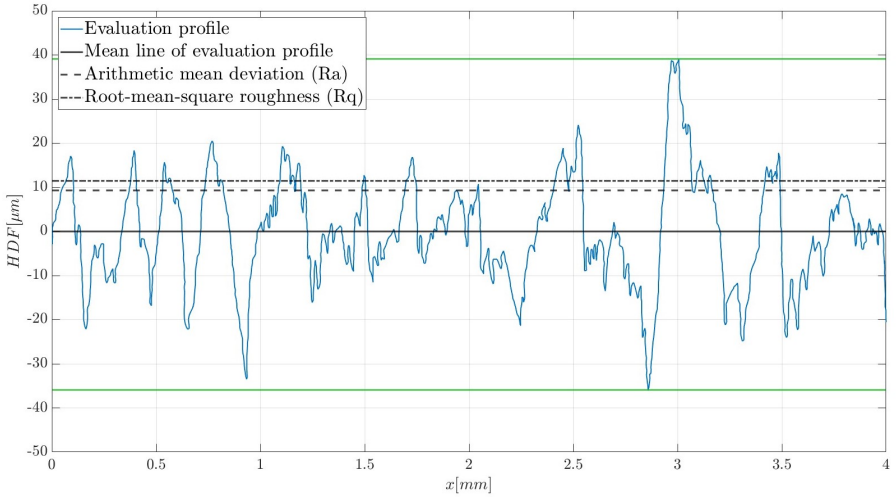


Figure 4 – Evaluation profile and statistical surface roughness parameters of the DemoP1 aerospike engine demonstrator sample.

Several approaches are available in the literature for the determination of the equivalent sand-grain roughness height, based on different statistical surface roughness parameters of the evaluation profile measured from the optical profilometry process on the AM metallic sample [43]. In the present numerical investigation, the equivalent sand-grain roughness height is imposed as $k_s = 59.17(\mu m)$. Assuming the surface roughness height remains constant, the relative equivalent sand-grain roughness, k_s/D_h, in different cross-sections across the longitudinal coordinate of the AM cooling channel is exhibited in Fig. 5. It is shown that the relative equivalent sand-grain roughness height is approximately 1.5 and 2 times higher at the throat region and inlet, respectively, in comparison with the remaining parts of the channel. This difference is attributed to the smaller fluidic width available at the throat region of the AM cooling channel, as exhibited in Fig. 3, for the satisfaction of the increased thermal load demands in high-heat flux aerospace applications such as the aerospike engine [28].

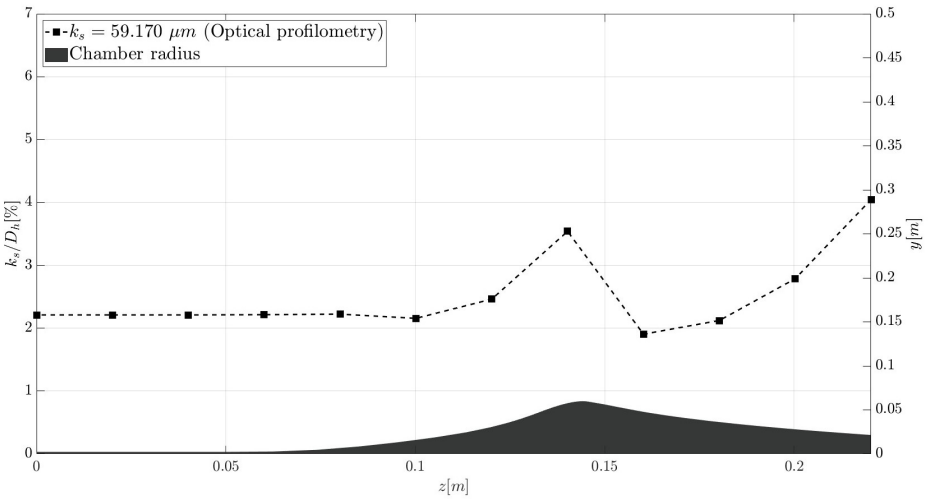


Figure 5 – Relative equivalent sand-grain roughness height at different cross-sections across longitudinal coordinate of coolant side.

The roughness height option for the wall boundaries on the ANSYS Fluent commercial CFD package is set equal to the equivalent-sand grain roughness height and the roughness constant is equal to 0.75 to account for the non-uniform distribution of the rough elements inherited by the AM process. To model roughness the approach based on the modification of the RANS boundary condition is per-

formed [44] by selecting the standard roughness option on the commercial CFD package. The high roughness (icing) approach [31] is also investigated in conjunction with the numerical simulation employing the two-equation $k-\omega$ SST model. This roughness modelling approach, strictly available for the $k-\omega$ SST model, is based on a correction on the Colebrook equation introduced by Aupoix [45].

2.4 Grid sensitivity analysis

A grid sensitivity analysis is performed for the determination of an appropriate grid size for the implementation of the required numerical simulations. The total number of cells for the coarse, intermediate and fine grid examined is reported in Table 3. The investigated test case considers the numerical simulation employing the two-equation $k-\omega$ SST model [33] with the standard roughness approach.

	Number of cells
Grid A (coarse)	0.87M
Grid B (intermediate)	1.3M
Grid C (fine)	2.6M

Table 3 – Number of cells for the grids investigated in the grid refinement study.

For the determination of an appropriate grid size the metric of interest regards a temperature profile at the midline of the AM cooling channel outlet starting from the heated bottom (basement) wall up to the adiabatic top wall boundary. The percentage error between the temperature profiles resulted from the CFD simulations employing the intermediate and the fine grid at each midline point is then computed. It can be seen in Fig. 6 that the percentage error between the CFD simulations is well below 1.5%. More specifically the mean error percentage computed between the numerical solution for the simulation with Grid B (intermediate) and Grid C (fine) is 0.41%. The fine grid is therefore selected for the implementation of the required numerical simulations in the AM cooling channel.

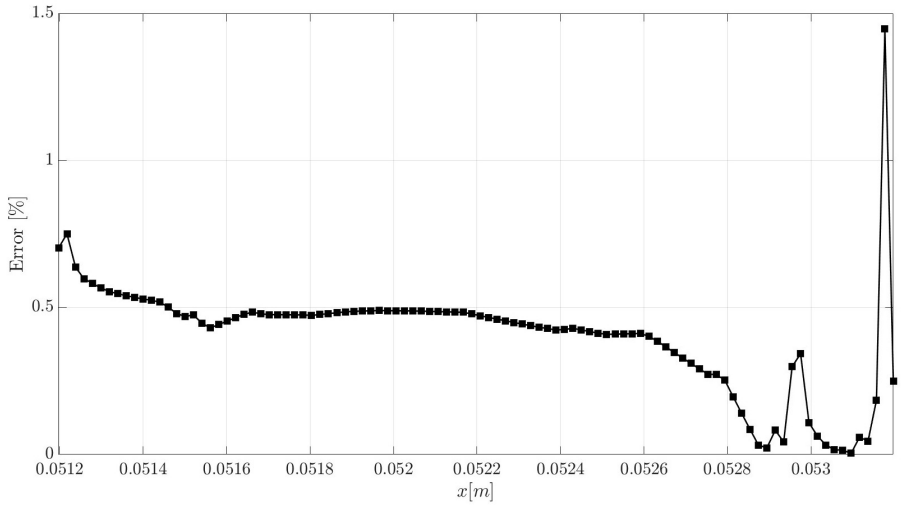


Figure 6 – Percentage error across basement-top wall midline of the outlet section of the AM cooling channel between simulations employing Grid B (intermediate) and Grid C (fine).

3. Results and discussion

In this section, the results from the simulations performed for the numerical solution of the liquid oxygen flow in the Additively Manufactured (AM) cooling channel of the DemoP1 aerospike engine demonstrator designed by Pangea Aerospace are reported. Different versions of the two-equation $k-\omega$ turbulence model and roughness modelling approaches on the commercial CFD package are investigated for their performance on the prediction of the flow-field characteristics of the coolant flow in the AM cooling channel: a) the standard (STD) two-equation $k-\omega$ [32], the baseline (BSL) $k-\omega$ [33] and the $k-\omega$ shear stress transport (SST) [33] turbulence models using the standard roughness approach and, b) the two-equation $k-\omega$ shear stress transport (SST) turbulence model [33] using the

high roughness (icing) approach [31] based on the correction on the Colebrook equation introduced by Aupoix [45]. The numerical solutions obtained using different variations of the two-equation $k-\omega$ turbulence model and roughness modelling options on the ANSYS Fluent software are compared against the temperature measurement available from the experimental campaign of the DemoP1 aerospike engine demonstrator at the outlet section of the AM cooling channel. The simulations have been performed on an Intel(R) Core(TM) i7-10700 at 2.90 GHz computer with 32GB RAM.

3.1 Numerical results

The numerical solutions obtained employing different variations of the two-equation $k-\omega$ turbulence model are compared against experimental data for the temperature at the outlet section of the Additively Manufactured (AM) cooling channel obtained from the hot-flow testing campaign of the DemoP1 engine. The average temperature value at the outlet section of the cooling channel is measured as $T_{out} = 305.07\ [K]$. The average bulk temperature of the coolant in different cross-sections of the AM cooling channel is presented in Fig. 7. As discussed the inlet section of the cooling channel is depicted at the right side, and the outlet section at the left side of the figures presented in this section. In Fig. 7 it is shown that the different variations of the two-equation $k-\omega$ turbulence model are capable of capturing the temperature gain observed, as the coolant is heated from the bottom (basement) wall boundary of the AM cooling channel while counterflowing from the base of the engine up to the injector plate of the aerospike engine demonstrator. The coolant enters the inlet section of the cooling channel at a cryogenic temperature of $T_{in} = 107.4\ [K]$. Note that in the CFD simulations the temperature at the inlet section of the AM cooling channel has been imposed as a uniform temperature profile. As discussed the temperature at the inlet section of the AM cooling channel was measured experimentally from the hot-flow testing campaign of the DemoP1 demonstrator. In Fig. 7 rapid bulk temperature changes are observed at the throat region for each of the numerical simulations performed employing different variations of the two-equation $k-\omega$ turbulence model. This adverse temperature gain is expected considering the geometric configuration of the engine and the higher heat flux applied at the throat region of the DemoP1 aerospike engine from the hot-gas side to the coolant side. Following the exit of the coolant from the throat region, a gradual increment of the bulk temperature is observed up to the outlet section of the AM cooling channel. The standard (STD) and the baseline (BSL) two-equation $k-\omega$ turbulence models appear to predict higher bulk temperature values across the length of the AM cooling channel in comparison with the $k-\omega$ SST variations.

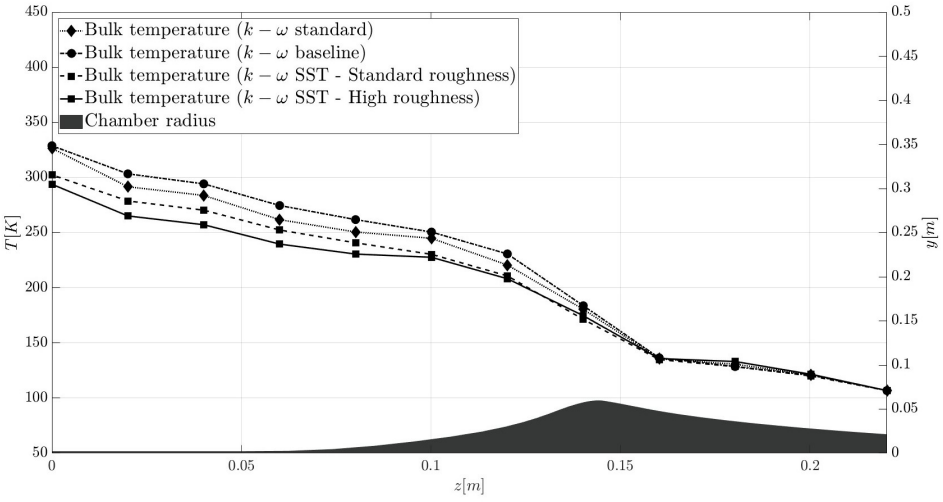


Figure 7 – Average bulk temperature at different cross-sections across longitudinal coordinate of coolant side for different numerical settings.

It is very important to quantify the steepness of the bulk temperature gain especially in the case when large variations are observed as the coolant counterflows within the throat region of the AM cooling channel. In Table 4 details on the average slope values of the bulk temperature gain at different parts of the cooling channel are reported. The AM cooling channel is divided into three sections: the

region from the channel inlet up to the beginning of the throat region, the throat region and the section from exit of the throat up to the outlet of the cooling channel. As shown in Table 4 the steepness of the temperature gain at the throat region is much higher in comparison with the remaining sections of the AM cooling channel and is clearly depicted for each numerical simulation utilising different variations of the two-equation $k-\omega$ turbulence model. The large differences in the average slope value between the throat region and the remaining sections of the cooling channel clearly indicate how rapidly temperature changes at the throat region of the DemoP1 aerospike engine demonstrator. As discussed this is a direct consequence of the increased thermal load applied at the specific area and is especially encountered in such high heat flux aerospace applications [28]. Note that the temperature change captured in the numerical simulations employing the standard (STD) and the baseline (BSL) $k-\omega$ turbulence models is steeper in comparison with the simulations utilising the standard [33] and the high roughness [45] (icing) approaches with the $k-\omega$ SST model.

Average slope value	$k-\omega$ STD [32]	$k-\omega$ BSL [33]	$k-\omega$ SST [33]	$k-\omega$ SST [45]
Channel inlet up to throat region beginning	479.22	493.43	468.09	482.97
Inside throat region	2123.88	2353.35	1894.87	1807.02
Throat region exit up to channel outlet	880.43	816.14	762.40	712.91

Table 4 – Bulk temperature gain steepness quantification in AM cooling channel of DemoP1 engine.

The numerically computed average bulk temperature value at the outlet section of the AM cooling channel is compared against the corresponding experimental value obtained from the hot-fire testing campaign of the DemoP1 aerospike engine demonstrator. The characteristics for the temperature gain across the AM cooling channel of the DemoP1 aerospike engine demonstrator in addition to the comparison of the obtained numerical solution against the experimental value for the coolant temperature at the outlet section of the channel are summarised in Table 5. The numerical simulation employing the standard (STD) two-equation $k-\omega$ turbulence model yields a temperature gain of $219.68\ [K]$, the simulation employing the baseline (BSL) two-equation $k-\omega$ turbulence model results in a temperature gain of $222\ [K]$, whilst the $k-\omega$ SST with the standard roughness modelling approach results in a temperature gain of $195.65\ [K]$ and the $k-\omega$ SST with the high roughness (icing) approach a temperature increment of $187.08\ [K]$. The average bulk temperature value at the outlet section of the AM cooling channel for each numerical simulation is also reported in Table 5. These values are compared against the measured value obtained from the experimental campaign of the DemoP1 aerospike engine demonstrator for the assessment of the performed numerical simulations. It is shown that the percentage error between the computed and the experimentally measured value of the coolant temperature at the outlet section of the AM cooling channel is 7.02% for the numerical simulation employing the standard $k-\omega$ turbulence model, 7.79% for the simulation employing the baseline $k-\omega$ turbulence model, 0.87% for the $k-\omega$ SST model with the standard roughness approach and 3.66% for the $k-\omega$ SST model with the high roughness (icing) approach. The percentage errors for the numerical simulation employing the two-equation $k-\omega$ SST turbulence model with either the standard [33] or the high roughness [45] (icing) modelling approach are within an acceptable range for industrial applications. The numerical simulations utilising the standard and the baseline two-equation $k-\omega$ turbulence models resulted in a percentage error in the range between 7% and 8% which, considering different uncertainty sources such as the inherited uncertainty from the measurement instrumentation of the experimental campaign, the uncertainty from the optical profilometry process, the numerical discretisation error and the uncertainty introduced by the regression model for the determination of the bottom wall thermal boundary condition, should not be discarded.

	$k-\omega$ STD [32]	$k-\omega$ BSL [33]	$k-\omega$ SST [33]	$k-\omega$ SST [45]
Total temperature gain $[K]$	219.68	222	195.65	187.08
Average outlet bulk temperature $[K]$	326.49	328.84	302.43	293.91
Error against experimental data	7.02%	7.79%	0.87%	3.66%

Table 5 – Temperature gain characteristics for coolant flow in AM cooling channel of DemoP1 engine.

In Fig. 8 the average coolant pressure in different cross-sections of the AM cooling channel of the DemoP1 aerospike engine demonstrator is shown. In terms of capturing the trend for the behavior of the coolant pressure across the AM cooling channel, the standard (STD) $k-\omega$ model, baseline (BSL) $k-\omega$ model and the $k-\omega$ SST model with both the standard and the high roughness (icing) modelling approach perform in a similar manner. Initially the coolant enters the channel at high pressure. The two-equation $k-\omega$ SST model utilising the high roughness (icing) approach predicts a coolant pressure at the inlet section of the channel approximately $10-20$ $[bar]$ lower than the other models. The numerical results for each performed simulation exhibit an adverse pressure drop within the throat region of the AM cooling channel. After exiting the throat region, a gradual reduction of the pressure of the coolant is observed for each test case investigated up to the outlet section of the AM cooling channel where a pressure outlet boundary condition has been imposed equal to the experimentally measured value obtained from the hot-flow testing of the DemoP1 aerospike engine.

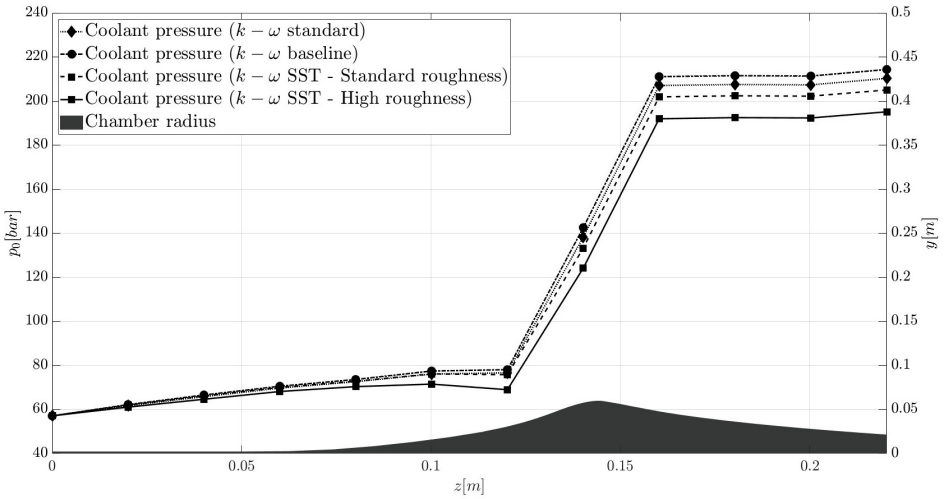


Figure 8 – Average coolant pressure at different cross-sections across longitudinal coordinate of coolant side for different numerical settings.

The pressure drop characteristics for the coolant flow in the Additively Manufactured (AM) cooling channel are summarised in Table 6. As expected the prediction of the two-equation $k-\omega$ SST model utilising the high roughness (icing) approach for a lower coolant pressure at the inlet section of the cooling channel results in a lower estimation of the total pressure drop. More specifically, the total pressure drop (ΔP) across the AM cooling channel is estimated as 153.19 $[bar]$ for the standard two-equation $k-\omega$ turbulence model, 157.21 $[bar]$ for the baseline $k-\omega$ turbulence model, 147.92 $[bar]$ for the $k-\omega$ SST model with the standard roughness modelling approach and 137.99 $[bar]$ for the $k-\omega$ SST turbulence model with the high roughness (icing) approach. The $k-\omega$ SST model with the high roughness (icing) approach [45] predicts a lower average coolant pressure at each cross-section across the AM cooling channel comparing with the other variations of the two-equation $k-\omega$ turbulence model investigated. The $k-\omega$ SST model with the standard roughness approach [33] also predicts lower coolant pressure values across the cooling channel in comparison with the standard (STD) and the baseline (BSL) $k-\omega$ turbulence models. The amount of pressure drop up to the exit of the throat region of the cooling channel is computed to be 133.63 $[bar]$, 136.24 $[bar]$, 129.25 $[bar]$ and 126.11 $[bar]$, respectively. Note that for each computational test case investigated more than 85% of the pressure drop is observed by the time the coolant exits the throat region of the AM cooling channel, which indicates the significance of the design considerations to be followed for the manufacturing of an aerospike engine AM cooling channel with a strong curvature at the throat region. The average velocity of the coolant in different cross-sections of the AM cooling channel is exhibited in Fig. 9. The numerical simulations performed for each variation of the two-equation $k-\omega$ turbulence model capture similar trends for the development of the velocity-field as the coolant is heated from the thermal load applied on the bottom (basement) wall of the cooling channel. More specifically, all simulations indicate that the coolant enters the AM channel with a relatively-low velocity of approxi-

	$k-\omega$ STD [32]	$k-\omega$ BSL [33]	$k-\omega$ SST [33]	$k-\omega$ SST [45]
Total ΔP across AM cooling channel $[bar]$	153.19	157.21	147.92	137.99
Amount of ΔP up to throat region exit $[bar]$	133.63	136.24	129.25	126.11
Percentage of total ΔP up to throat region exit	87.23%	86.66%	87.38%	91.39%

Table 6 – Pressure drop characteristics for coolant flow in AM cooling channel of DemoP1 engine.

mately $30\ [ms^{-1}]$ when a significant acceleration is observed within the throat region of the channel. The behavior of the coolant with respect to its velocity is justified on the basis of the reduction of the cross-section area and, as a result, the fluidic width available in the throat region. As discussed, the additive manufacturing of the cooling channel with a variable cross-section area is intended for the satisfaction of the increased thermal demands at the throat due to the higher heat flux applied in the region in comparison with the remaining sections of the channel [28]. Following the exit of the coolant from the throat region of the AM cooling channel, the coolant slightly decelerates and a momentum recovering is observed as the coolant moves towards the outlet section of the cooling channel. Note that the $k-\omega$ SST turbulence model with the high roughness [45] (icing) approach predicts higher coolant velocity values at the different cross-sections across the AM cooling channel, whilst small deviations are observed between the coolant velocity values obtained from the simulations employing the STD [32], BSL [33] and the SST model with the standard roughness approach.

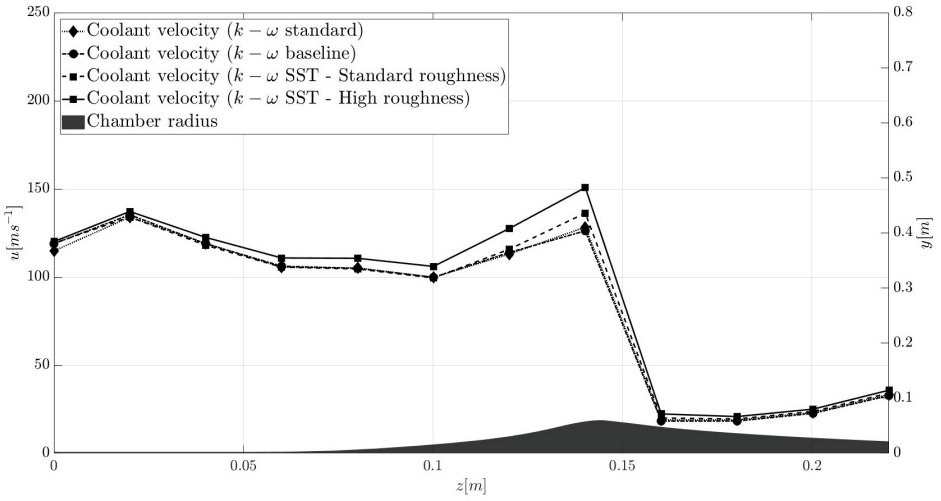


Figure 9 – Average coolant velocity at different cross-sections across longitudinal coordinate of coolant side for different numerical settings.

In Fig. 10 details on the average density of the coolant in different cross-sections of the AM cooling channel are reported. The behavior of each turbulence model for the description of the coolant density across the cooling channel is comparable. It is shown that the numerical simulation employing the two-equation $k-\omega$ SST turbulence model with the high roughness (icing) modelling approach predicts a lower average density of the fluid at the inlet section of the AM cooling channel in comparison with the remaining turbulence models investigated. At the throat region of the cooling channel which is admittedly the most challenging section of the channel in terms of both the strong curvature and the higher relative equivalent sand-grain roughness height, each numerical simulation captures an adverse reduction of the density property of the fluid. After exiting the throat region the reduction of the fluid density until the coolant reaches the outlet section of the AM cooling channel is gradual with all numerical simulations performed predicting an average outlet density value below $80\ [kgm^{-3}]$. Note that significant deviations in the estimation of the coolant density between the employed variations of the two-equation $k-\omega$ turbulence models are observed only up to the middle of the throat region. From the throat region middle up to the outlet section of the cooling channel the numerical simulations utilising the standard (STD) $k-\omega$ turbulence model [32], baseline (BSL) $k-\omega$ turbulence model [33] and the $k-\omega$ SST models in conjunction with both the standard [33] and the high roughness [45]

(icing) approach perform in a similar manner in terms of capturing the coolant density.

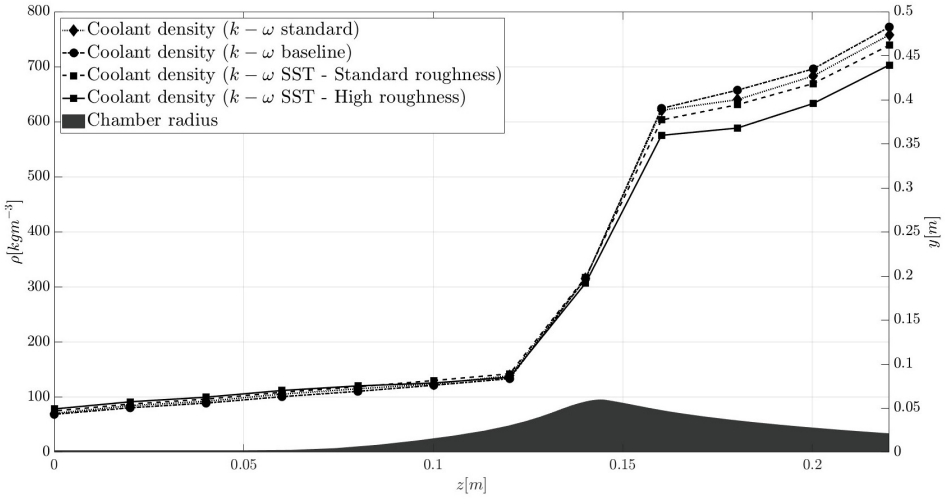


Figure 10 – Average coolant density at different cross-sections across longitudinal coordinate of coolant side for different numerical settings.

4. Conclusions

In the present work a numerical investigation for the performance of different variations of the two-equation $k-\omega$ turbulence model has been performed for the numerical solution of the cryogenic LOx flow in an Additively Manufactured (AM) cooling channel of the DemoP1 LOx/LNG aerospike engine demonstrator designed by Pangea Aerospace. The geometric configuration of the AM cooling channel is a three-dimensional curvilinear cooling channel of variable, rectangular cross-section with a strong curvature at the throat region of the aerospike engine demonstrator. For the assessment of the turbulence models employed for the closure of the governing equations and the determination of the turbulent transport equations the following models have been examined: a) the standard (STD) two-equation $k-\omega$ turbulence model [32], b) the baseline (BSL) two-equation $k-\omega$ turbulence model [33], c) the two-equation $k-\omega$ shear stress transport (SST) turbulence model [33] using a standard roughness modelling approach and d) the two-equation $k-\omega$ SST turbulence model in conjunction with the high roughness (icing) modelling approach [31] which is based on a correction of the Colebrook equation introduced by Aupoix [45]. The study focuses on the determination of the efficient formulations and turbulence models for the RANS closure problem for the accurate prediction of the spatial development of the primitive variables such as the coolant temperature, pressure, velocity and density in different cross-sections across the AM cooling channel of the DemoP1 aerospike engine.
The numerical solutions performed for the characterisation of the heat transfer and pressure drop characteristics in the AM cooling channel utilising different variations of the two-equation $k-\omega$ turbulence model are compared against experimental data provided from Pangea Aerospace for the full-scale single-injector element hot-fire test campaign of the DemoP1 aerospike engine demonstrator. The comparison is implemented through the estimation of a percentage error between the numerical and the experimentally measured value of the coolant temperature at the outlet section of the AM cooling channel. The percentage errors for the numerical simulation employing the two-equation $k-\omega$ SST turbulence model in conjunction with both the standard [33] and the high roughness [45] (icing) approach are acceptable and below a threshold value for industrial applications of 5%. The numerical solutions obtained from the utilisation of the standard (STD) and the baseline (BSL) two-equation $k-\omega$ turbulence model resulted in a percentage error within $7\%-8\%$ which, accounting for different uncertainty sources (experimental, numerical, statistical, etc.) should not be discarded.

5. Acknowledgements

The present research work was financially supported by the Centre for Propulsion and Thermal Power Engineering and the Cranfield Air and Space Propulsion Institute (CASPI) at Cranfield University, UK

in collaboration with Pangea Aerospace, Spain. The authors would also like to acknowledge the IT support and the use of the High Performance Computing (HPC) facilities at Cranfield University, UK.

6. Contact Author Email Address

The main author can be contacted at nikos.monokrousos@cranfield.ac.uk

7. Data availability statement

The data that support the findings of this study are available from the corresponding author upon request.

8. Conflict of interest statement

The authors declare no conflict of interest.

9. Copyright Statement

The authors confirm that they, and/or their company or organization, hold copyright on all of the original material included in this paper. The authors also confirm that they have obtained permission, from the copyright holder of any third party material included in this paper, to publish it as part of their paper. The authors confirm that they give permission, or have obtained permission from the copyright holder of this paper, for the publication and distribution of this paper as part of the ICAS proceedings or as individual off-prints from the proceedings.

References

[1] Weiss P-É, Deck S, Robinet J-C and Sagaut P. On the dynamics of axisymmetric turbulent separating/reattaching flows. *Physics of Fluids*, Vol. 21, No. 7, pp 075103, 2009. https://doi.org/10.1063/1.3177352

[2] Statnikov V, Sayadi T, Meinke M, Schmid P and Schröder W. Analysis of pressure perturbation sources on a generic space launcher after-body in supersonic flow using zonal turbulence modeling and dynamic mode decomposition. *Physics of Fluids*, Vol. 27, No. 1, pp 016103, 2015. https://doi.org/10.1063/1.4906219

[3] Deprés D, Reijasse P and Dussauge J P. Analysis of Unsteadiness in Afterbody Transonic Flows. *AIAA Journal*, Vol. 42, No. 12, pp 2541-2550, 2004. https://doi.org/10.2514/1.7000

[4] Jian D and Qiuru Z. Key technologies for thermodynamic cycle of precooled engines: A review. *Acta Astronautica*, Vol. 177, pp 299-312, 2020. https://doi.org/10.1016/j.actaastro.2020.07.039

[5] Fernández-Villacé V and Paniagua G. Simulation of a Combined Cycle for High Speed Propulsion. *48th AIAA Aerospace Sciences Meeting Including the New Horizons Forum and Aerospace Exposition*, Orlando, Florida, 2010. https://doi.org/10.2514/6.2010-1125

[6] Tsentis S E, Gkoutzamanis V G, Gaitanis A D. and Kalfas A I. Multi-platform app-embedded model for hybrid air-breathing rocket-cycle engine in hypersonic atmospheric ascent. *The Aeronautical Journal*, Vol. 125, No. 1291, pp 1631–1653, 2021. https://doi.org/10.1017/aer.2021.3

[7] Tsentis S, Goulos I, Prince S, Pachidis V and Zmijanovic V. Propulsion Aerodynamics for a Novel High-Speed Exhaust System. *ASME Journal of Engineering for Gas Turbines and Power*, Vol. 145, No. 12, pp 121011, 2023. https://doi.org/10.1115/1.4063416

[8] Scharnowski S and Kähler C J. Investigation of the base flow of a generic space launcher with dual-bell nozzle. *CEAS Space Journal*, Vol. 13, pp 197–216, 2021. https://doi.org/10.1007/s12567-020-00333-5

[9] Tsentis S, Goulos I, Prince S, Pachidis V, Zmijanovic V and Saavedra J. Wind Tunnel Installation Effects on the Base Flow for a High-Speed Exhaust System. *AIAA SCITECH 2024 Forum*, Orlando, Florida, 2024. https://doi.org/10.2514/6.2024-1774

[10] Gradl P R, Protz C S, Cooper K, Ellis D L, Evans L J and Garcia C. GRCop-42 Development and Hot-fire Testing Using Additive Manufacturing Powder Bed Fusion for Channel-cooled Combustion Chambers. *AIAA Propulsion and Energy 2019 Forum*, Indianapolis, Indiana, 2019. https://doi.org/10.2514/6.2019-4228

[11] Favero G, Bonesso M, Rebesan P, Dima R, Pepato A and Mancin S. Additive manufacturing for thermal management applications: from experimental results to numerical modeling. *International Journal of Thermofluids*, Vol. 10, pp 100091, 2021. https://doi.org/10.1016/j.ijft.2021.100091

[12] Zhang C, Wang S, Li J, Zhu Y, Peng T and Yang H. Additive manufacturing of products with functional fluid channels: A review. *Additive Manufacturing*, Vol. 36, pp 101490, 2020. https://doi.org/10.1016/j.addma.2020.101490

[13] Soleimani S and Eckels S. A review of drag reduction and heat transfer enhancement by riblet surfaces in closed and open channel flow. *International Journal of Thermofluids*, Vol. 9, pp 100053, 2021. https://doi.org/10.1016/j.ijft.2020.100053

[14] Demeneghi G, Barnes B, Gradl P R, Mayeur J R and Hazeli K. Size effects on microstructure and mechanical properties of additively manufactured copper-chromium-niobium alloy. *Materials Science and Engineering A*, Vol. 820, pp 141511, 2021. https://doi.org/10.1016/j.msea.2021.141511

[15] Kerstens F, Cervone A and Gradl P R. End to end process evaluation for additively manufactured liquid rocket engine thrust chambers. *Acta Astronautica*, Vol. 182, pp 454-465, 2021. https://doi.org/10.1016/j.actaastro.2021.02.034

[16] Stimpson C K, Snyder J C, Thole K A and Mongillo D. Roughness Effects on Flow and Heat Transfer for Additively Manufactured Channels. *Journal of Turbomachinery*, Vol. 138, No. 5, 2016. https://doi.org/10.1115/1.4032167

[17] Morshed-Behbahani K, Aliyu A, Bishop D P and Nasiri A. Additive manufacturing of copper-based alloys for high-temperature aerospace applications: A review. *Materials Today Communications*, Vol. 38, pp 108395, 2024. https://doi.org/10.1016/j.mtcomm.2024.108395

[18] Cooper K G, Lydon J D, LeCorre M D, Jones Z C, Scannapieco D S, Ellis D L and Lerch B A. Three-dimensional printing GRCop-42. *NASA Technical Memorandum (TM)*, NASA, 2018.

[19] Chen Y, Zeng C, Ding H, Emanet S, Gradl P R, Ellis D L and Guo S. Thermophysical properties of additively manufactured (AM) GRCop-42 and GRCop-84. *Materials Today Communications*, Vol. 36, pp 106665, 2023. https://doi.org/10.1016/j.mtcomm.2023.106665

[20] Tang X, Chen X, Sun F, Liu P, Zhou H and Fu S. The current state of CuCrZr and CuCrNb alloys manufactured by additive manufacturing: A review. *Materials & Design*, Vol. 224, pp 111419, 2022. https://doi.org/10.1016/j.matdes.2022.111419

[21] Votta R, Battista F, Ferraiuolo M, Roncioni P, Salvatore V and De Matteis P. Design of an Experimental Campaign on Methane Regenerative Liquid Rocket Engine Cooling System. *49th AIAA/ASME/SAE/ASEE Joint Propulsion Conference*, Orlando, Florida, 2013. https://doi.org/10.2514/6.2013-4146

[22] Pizzarelli M, Nasuti F, Onofri M, Roncioni P, Votta R and Battista F. Heat transfer modeling for supercritical methane flowing in rocket engine cooling channels. *Applied Thermal Engineering*, Vol. 75, pp 600-607, 2015. https://doi.org/10.1016/j.applthermaleng.2014.10.008

[23] Ricci D, Natale P and Battista F. Experimental and numerical investigation on the behaviour of methane in supercritical conditions. *Applied Thermal Engineering*, Vol. 107, pp 1334-1353, 2016. https://doi.org/10.1016/j.applthermaleng.2016.07.052

[24] Votta R, Battista F, Salvatore V, Pizzarelli M, Leccese G, Nasuti F and Meyer S. Experimental investigation of transcritical methane flow in rocket engine cooling channel. *Applied Thermal Engineering*, Vol. 101, pp 61-70, 2016. https://doi.org/10.1016/j.applthermaleng.2015.12.019

[25] Latini B, Fiore M and Nasuti F. Modeling liquid rocket engine coolant flow and heat transfer in high roughness channels. *Aerospace Science and Technology*, Vol. 126, pp 107672, 2022. https://doi.org/10.1016/j.ast.2022.107672

[26] Stimpson C K, Snyder J C, Thole K A and Mongillo D. Scaling Roughness Effects on Pressure Loss and Heat Transfer of Additively Manufactured Channels. *Journal of Turbomachinery*, Vol. 139, No. 2, 2017. https://doi.org/10.1115/1.4034555

[27] Ghidini T, Grasso M, Gumpinger J, Makaya A and Colosimo B M. Additive manufacturing in the new space economy: Current achievements and future perspectives. *Progress in Aerospace Sciences*, Vol. 142, pp 100959, 2023. https://doi.org/10.1016/j.paerosci.2023.100959

[28] Rossi F, Esnault G, Sápi Z, Palumbo N, Argemí A and Bergström R. Research Activities in the Development of DemoP1: A LOX/LNG Aerospike Engine Demonstrator. *7th Edition of the Space Propulsion Conference*, Virtual, 2021.

[29] Fadigati L, Rossi F, Souhair N, Ravaglioli V and Ponti F. Development and simulation of a 3D printed liquid oxygen/liquid natural gas aerospike. *Acta Astronautica*, Vol. 216, pp 105-119, 2024. https://doi.org/10.1016/j.actaastro.2023.12.037

[30] Rossi F, Sápi Z, Palumbo N, Demediuk A and Ampudia M. Manufacturing and Hot-Fire Test Campaign of the DemoP1 Aerospike Engine Demonstrator. *8th Edition of the Space Propulsion Conference*, Estoril, Portugal, 2022.

[31] Ansys Fluent User's Guide. *ANSYS 2023 R2*. Ansys Inc., Canonsburg, PA, 2023.

[32] Wilcox D C. *Turbulence Modeling for CFD*. 2nd edition. DCW Industries, Inc. La Canada, California, 1998.

[33] Menter F R. Two-equation eddy-viscosity turbulence models for engineering applications. *AIAA Journal*, Vol. 32, No. 8, pp 1598-1605, 1994. https://doi.org/10.2514/3.12149

[34] Menter F R. Review of the shear-stress transport turbulence model experience from an industrial perspective. *International Journal of Computational Fluid Dynamics*, Vol. 23, No. 4, pp 305–316, 2009. https://doi.org/10.1080/10618560902773387

[35] Cahill J A and Kirshenbaum A D. The density of liquid copper from its melting point (1356°K.) to 2500°K and an estimate of its critical constants. *The Journal of Physical Chemistry*, Vol. 66, No. 6, pp 1080-1082, 1962. https://doi.org/10.1021/j100812a027

[36] Thurnay K. Thermal properties of transition metals. *Materials Science, Physics, Chemistry*, 1998. doi: 10.5445/IR/270043419

[37] Chase M W Jr. NIST-JANAF Thermochemical Tables, Fourth Edition. *Journal of Physical and Chemical Reference Data*, Monograph 9, pp 1-1951, 1998.

[38] National Institute of Standards and Technology (NIST). *NIST Standard Reference Database Number 69*. NIST Chemistry WebBook, 2023. https://doi.org/10.18434/T4D303

[39] Ho C Y, Powell R W and Liley P E. Thermal Conductivity of the Elements. *Journal of Physical and Chemical Reference Data*, Vol. 1, No. 2, pp 279–421, 1972. https://doi.org/10.1063/1.3253100

[40] Roe P L. Approximate Riemann solvers, parameter vectors, and difference schemes. *Journal of Computational Physics*, Vol. 43, No. 2, pp 357-372, 1981. https://doi.org/10.1016/0021-9991(81)90128-5

[41] The MathWorks, I. *Curve Fitting Toolbox*. Natick, Massachusetts, United State, 2020. Retrieved from https://www.mathworks.com/products/curvefitting.html

[42] Leach R. *Characterisation of Areal Surface Texture*. Springer Berlin, Heidelberg, 2013. https://doi.org/10.1007/978-3-642-36458-7

[43] Brackbill T P and Kandlikar S G. Effects of Roughness on Turbulent Flow in Microchannels and Minichannels. *ASME 2008 6th International Conference on Nanochannels, Microchannels, and Minichannels*. Darmstadt, Germany, pp. 1179-1186, 2008. https://doi.org/10.1115/ICNMM2008-62224

[44] Kadivar M, Tormey D and McGranaghan G. A comparison of RANS models used for CFD prediction of turbulent flow and heat transfer in rough and smooth channels. *International Journal of Thermofluids*, Vol. 20, pp 100399, 2023. https://doi.org/10.1016/j.ijft.2023.100399

[45] Aupoix B. Roughness Corrections for the $k-\omega$ Shear Stress Transport Model: Status and Proposals. *ASME. Journal of Fluids Engineering*, Vol. 137, No. 2, pp 021202, 2015. https://doi.org/10.1115/1.4028122



https://dspace.org/

Numerical solution of LOx flow in a liquid rocket engine additively manufactured cooling channel

Monokrousos, Nikos; Könözsy, László Z. ; Pachidis, Vassilios; Sozio, Ernesto; Rossi, Federico

2024-10-08
International Council of the Aeronautical Sciences (ICAS)
https://www.icas.org/ICAS_ARCHIVE/ICAS2024/data/papers/ICAS2024_0105_paper.pdf
Monokrousos N, Konozsy L, Pachidis V, et al., (2024) Numerical solution of LOx flow in a liquid rocket engine additively manufactured cooling channel. ICAS Proceedings. 34th Congress of the International Council of the Aeronautical Sciences, 9-12 September 2024, Florence, Italy

Downloaded from a DSpace repository. https://dspace.org/